

## MODELING ON-SUN TESTS OF A PROTOTYPE SOLID PARTICLE RECEIVER FOR CONCENTRATING SOLAR POWER PROCESSES AND STORAGE

Clifford K. Ho, Siri S. Khalsa, and Nathan P. Siegel  
Solar Technologies Department, Sandia National Laboratories  
P.O. Box, 5800, Albuquerque, NM 87185-1127, USA  
(505) 844-2384, [ckho@sandia.gov](mailto:ckho@sandia.gov)

### ABSTRACT

A model has been developed to simulate the performance of a prototype solid particle receiver that was recently tested at Sandia National Laboratories. The model includes irradiation from the concentrated solar flux, two-band re-radiation and emission with the cavity, discrete-phase particle transport and heat transfer, gas-phase convection, wall conduction, and radiative and convective heat losses. Simulated temperatures of the particles and cavity walls were compared to measured values for nine on-sun tests. Results showed that the simulated temperature distributions and receiver efficiencies matched closely with trends in experimental data as a function of input power and particle mass flow rate. The average relative error between the simulated and measured efficiencies and increases in particle temperature was less than 10%. Simulations of particle velocities and concentrations as a function of position beneath the release point were also evaluated and compared to measured values collected during unheated tests with average relative errors of 6% and 8%, respectively. The calibrated model is being used in parametric analyses to better understand the impact and interactions of multiple parameters with a goal of optimizing the performance and efficiency of the solid particle receiver.

### 1. INTRODUCTION

Advanced solar-based power cycles and thermochemical fuel production processes require thermal energy input with high temperatures in excess of 800°C. Conventional central receiver technologies are capable of reaching a maximum heat input temperature of around 600°C [1]. However, direct absorption receivers using solid particles that fall through a beam of concentrated solar energy for heat absorption and storage have the potential to increase the maximum temperature of the heat-transfer media to over 1,000°C. Other reactor designs have been developed for high-temperature solid-gas

reactions [2], [3], [4], but the falling particle receiver appears well-suited for scalability and larger-scale energy production [5].

Sandia National Laboratories recently designed and tested a prototype solid particle receiver. Particles were released at the top of the solid particle receiver and exposed to concentrated sunlight. Tests were performed with concentrating solar power ranging from approximately 1.6 –2.5 MW. This paper describe a computational fluid dynamics model that was developed to simulate the performance of these tests. The objective was to develop a validated model that could be used to guide and optimize the design of next-generation solid particle receivers. A significant difference between the current analysis and previous analyses of solid particle receivers is that this is the first time comparisons have been made to on-sun tests in a large-scale system with concentrated light from a heliostat field. Hruby et al. [6] perform heating tests of falling particles, but the heat was from a uniform source of tungsten-filament infrared lamps. Rigorous numerical analysis of these tests was performed by Evans et al. [7], but the model was only two dimensional. Analytical models of radiative heat transfer and convective losses in a solid particle receiver were developed by Falcone et al. [8], but interaction between the falling particles and the continuous gas phase was neglected (i.e., no entrainment of air by the particles was simulated, and, hence, the air convection and impact on wall and particle temperatures was not rigorously simulated. Chen et al. [9] recently developed a computational fluid dynamics model of a solid particle receiver, but the solar-load model that was used did not irradiate the particles directly as discussed in Section 3.3. Their model was also not validated to on-sun tests.

The three-dimensional model developed in this paper includes irradiation from the concentrated solar flux, two-band re-radiation and emission within the cavity, discrete-phase particle transport and heat transfer (convection and radiation),

gas-phase buoyancy and convection with two-way turbulence interaction with the particles, wall conduction, and radiative and convective heat losses. Comparisons between the simulated and measured cavity efficiencies and temperatures of the particles and cavity walls were evaluated. Comparisons between simulated and measured particle velocities and concentrations during unheated tests were also performed.

input power, which was calculated using DELSOL [12], was recently revised and is slightly different for each test than the values reported in [11].

**Table 1. Summary of on-sun tests [11]. Mass flow rate expressed per meter of injection width (see Figure 2). Input power modified from [11] using updated DELSOL [12] results.**

Date	Direct Normal Insolation (W/m <sup>2</sup> )	Particle Mass Flow Rate (kg/s-m)	Input Power (MW <sub>th</sub> )
2/8/2008	1050	8.72	2.02
2/8/2008	1070	8.72	2.42
2/11/2008	1002	5.32	1.58
2/11/2008	1038	5.32	2.32
2/11/2008	1040	3.84	2.42
2/13/2008	1050	3.84	1.76
2/18/2008	1000	8.72	2.48
2/22/2008	962	5.32	2.39
2/28/2008	953	3.84	2.51

## 2. PREVIOUS TESTING

In recent years, tests have been performed at Sandia National Laboratories to characterize the performance of a prototype solid particle receiver. Siegel et al. [10] performed unheated tests to evaluate the velocity distribution and concentration of a particle “curtain” as the particles were released from a discharge slot to a collection point several meters below. Siegel and Kolb [11] performed nine on-sun tests with varying particle flow rates and different amounts of concentrated solar power. Figure 1 shows a photograph and drawing of the prototype solid particle receiver tested at Sandia National Laboratories.

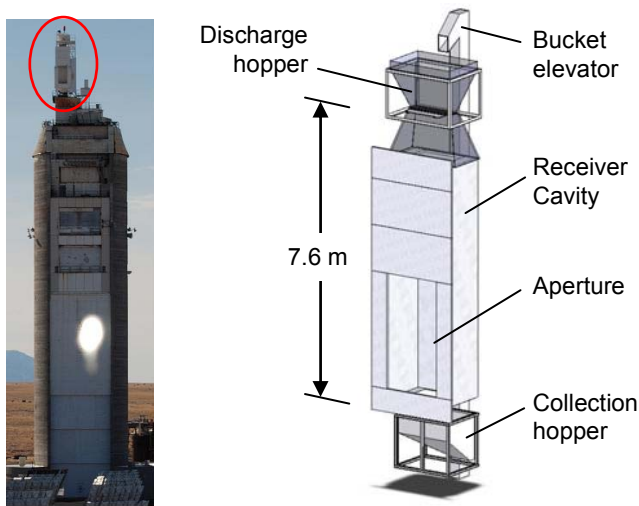


**Figure 1. Photo and drawing of the solid particle receiver tested at Sandia National Laboratories.**

The solid particle receiver was tested on top of Sandia’s 61 m tall central receiver at the National Solar Thermal Test Facility (NSTTF) in Albuquerque, NM. The heliostat field at the NSTTF can provide up to an estimated 5 MW<sub>th</sub> from 212 heliostats, each with an area of 37 m<sup>2</sup>. The dimensions of the receiver cavity are 6.3 m high by 1.85 m wide by 1.5 m deep. Particles were released from a discharge hopper above the cavity and allowed to fall through the cavity where the particle were irradiated by a concentrated solar flux aimed at the aperture in the front of the cavity. The solar power entering the aperture was calculated using measured direct normal insolation values and the number and position of heliostats used in each test. Table 1 summarizes the on-sun tests. The

The interior and front of the receiver were covered with 5 cm of Duraboard HD ([www.unifrax.com](http://www.unifrax.com)), an alumina-silica ceramic fiber board, to protect and insulate the receiver. The emissivity of alumina silica powders exhibits a two-band spectral dependence with a low emissivity (~0.2) below ~4.5 microns and a high emissivity (~0.8) above ~4.5 microns [13]. This requires a two-band radiation model to correctly account for both the high solar reflectivity (low emissivity) at lower wavelengths and high thermal emission at higher wavelengths. Table 2 summarizes the properties of Duraboard HD.

**Table 2. Duraboard HD properties.**

Property	Value
Density (kg/m <sup>3</sup> )	420
Melting point (°C)	1760
Thermal conductivity (W/m-K)	0.075 – 0.22 (200°C – 980°C)
Specific heat (J/kg-K)	1000
Emissivity	0.2 (< 4.5 microns) 0.8 (> 4.5 microns)

The solid particles used in the tests were CARBO HSP 20/40 (82% Al<sub>2</sub>O<sub>3</sub>, 5% SiO<sub>2</sub>, 3.5% TiO<sub>2</sub>) with ~7% iron oxide that gives the particles a black appearance ([www.carboceramics.com](http://www.carboceramics.com)). Table 3 summarizes the properties of the CARBO HSP particles.

**Table 3. CARBO HSP particle properties.**

Property	Value
Density (kg/m <sup>3</sup> )	3560
Median diameter (microns)	697
Estimated thermal conductivity (W/m-K)	2.0
Estimated specific heat* (J/kg-K)	$-1.12e-3T^2 + 2.07T + 264$
Estimated emissivity	0.8
Sphericity	0.9

\*Quadratic curve fit for specific heat of Al<sub>2</sub>O<sub>3</sub>, where T is the average particle temperature in Kelvin [14].

Temperatures in the discharge hopper, collection hopper, and at various points along the walls were recorded using Type K thermocouples.

### 3. COMPUTATIONAL APPROACH

A computational fluid dynamics model was developed using FLUENT [15] to simulate the coupled processes of gas flow, particle flow, solar irradiation, and heat transfer within the solid particle receiver. Figure 2 shows the model of the solid particle receiver that was used in FLUENT. Sensitivity studies of flow within the cavity were performed using different numbers of hexahedral elements (up to ~1 million), and it was found that a mesh resolution with 169,200 cells was sufficient to yield grid independence.

#### 3.1 Gas Flow Model

As the particles fall through the receiver, air is entrained into the particle flow. Cool air from outside the receiver cavity is pulled into the receiver and circulated within the hot cavity. FLUENT solves the governing partial differential equations for gas-phase conservation of mass, momentum, and energy [15].

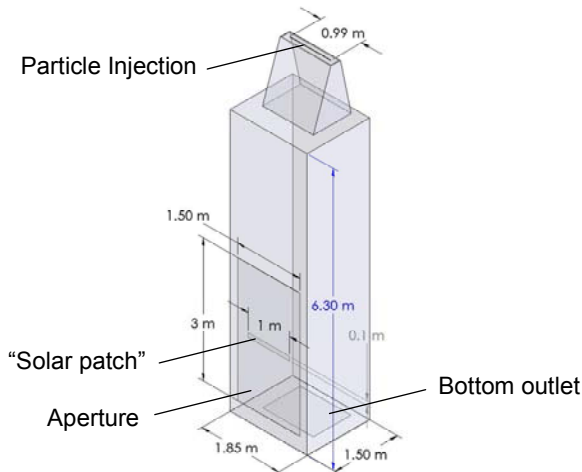


**Figure 2. Drawing of the model used in FLUENT.**

Turbulent flow (and closure for the turbulent viscosity term) was modeled using the k-ε realizable turbulence model (using default values) with the standard wall function, which provides a commonly used approximation for the near-wall velocity for turbulent flows. The effects of buoyancy are included in the turbulence model. The term “realizable” refers to the fact that the model satisfies mathematical constraints on the Reynolds stresses (must remain positive) by making a previously defined constant in the definition of the turbulent viscosity a function of the mean flow and turbulence quantities. Neither the standard k-ε model nor the RNG k-ε model is realizable and can violate the positive value of the Reynolds stress terms. The realizable k-ε model has been validated for a wide range of flows including jets, mixing layers, channel and boundary layer flows, and separated flows [16]. The realizable k-ε model is likely to provide superior performance flow flows involving rotation, boundary layers with strong adverse pressure gradients, separation, and recirculation [15].

Surfaces representing the aperture and bottom outlet of the receiver were specified as fixed pressure boundaries where air could enter and exit (see Figure 2).

#### 3.2 Particle Flow Model

The motion of the particles falling through the receiver is governed in FLUENT by a time-integrated force balance on each particle that relates particle acceleration, drag, and gravity in a Lagrangian reference frame. The formulation assumes that the interaction between particles is negligible, which is valid for particle volume fractions less than approximately 10%. Previous tests of falling particles have shown that the particle volume fraction (volume of particles divided by total volume occupied by particles and air) is less than several percent [10]. However, the particles do interact with the continuous gas phase and entrain air as they fall through the receiver. Two-way turbulence coupling was activated in FLUENT.

The particles were released from 300 points defined by the narrow slot at the top of the receiver (see Figure 2). The inlet temperature of the particles was prescribed based on measured discharge temperatures. The mass flow rate of the particles was also prescribed (Table 1), and this value was used in FLUENT to determine the rate of particle release (particles/second) based on the mass of each particle and the number of release points. Sensitivity studies showed that the number and location of release points defined along the slot did not significantly impact the results as long as the number of release points was greater than 100. A surface representing the bottom opening of the cavity, as well as the aperture in the front of the receiver, were defined as outlets where particles could escape (see Figure 2). All other wall surfaces were defined as reflecting surfaces for the solid particles.

Convection and radiative heat transfer (discrete ordinates radiation) were also included in the discrete-phase particle model. The particles were assumed to be spherical, and the particle radiation scattering factor in FLUENT was assumed to

be 0.3. The particles absorb irradiation, reducing the amount of solar flux that reaches the walls of the receiver. The mass flow rate of the particles, which impacts the particle concentration, also impacts the amount of irradiation received by the particles and cavity walls. Particles also emit thermal radiation.

### 3.3 Solar Irradiation and Heat Transfer Models

A discrete-ordinates radiation model in FLUENT [15] was used to simulate the solar irradiation onto the falling particles from the heliostat field. The discrete-ordinates radiation model solves the radiative transfer equation over a domain of discrete solid angles. The model does not perform ray tracing; instead, the radiative transfer equation is transformed into as many transport equations as there are solid angles. It calculates the radiation intensity as a result of absorption, scattering, and emission within the fluid, along with reflection and emission from surfaces. The solution method is the same as that used for the momentum and energy equations.

This approach is an improvement over previous modeling of a solid particle receiver by Chen et al. [9]. In that study, a solar ray-tracing algorithm in FLUENT [15] was used to predict the solar illumination energy on the walls. In Chen et al. [9], heating of the falling particles was simulated by reradiation from the walls to the particles, but direct irradiation from the heliostat beams was not modeled since the solar ray-tracing solar-load model does not interact directly with the discrete-phase particles. In contrast, the use of the discrete-ordinates radiation model to apply the solar load on the model domain allows for direct irradiation of the particles.

In the current study, a small “solar patch” was applied in the middle of the aperture to simulate the concentrated solar irradiation entering the receiver via the discrete-ordinates radiation model. The beam width, direction, and diffuse fraction of the irradiation received through the solar patch were used as calibration parameters. The diffuse fraction (between 0 and 1) dictates how much radiation from the solar patch is emitted specularly (along the beam direction) or diffusely (in all directions from the surface). The magnitude of the solar irradiation [ $\text{W}/\text{m}^2$ ] applied to the solar patch was calculated using the estimated input power [MW] for each test from Table 1 and the size of the solar patch ( $0.1 \text{ m}^2 - 1 \text{ m}^2$ ). The entire solar irradiation was applied to a single wavelength band (0 – 4.5 microns) in a two-band model in FLUENT. The second wavelength band (4.5 – 100 microns) was used to account for the higher thermal emission at higher wavelengths from the cavity walls (see Section 2 regarding the two-band spectral emissivity of Duraboard HD).

Heat conduction was also simulated within the walls of the cavity, and convective heat loss to the ambient was simulated assuming a heat transfer coefficient of  $5 \text{ W}/\text{m}^2\text{-K}$  and a free-stream temperature of 300 K on the outside of the walls.

The temperature of the aperture boundary surface was set equal to the measured ambient temperature during each test. This temperature was used as a blackbody boundary temperature (with an emissivity of one) to calculate reradiation

from the internal walls of the cavity to the aperture (and bottom outlet). Sensitivity studies were performed and showed that the use of a variable ambient temperature (relative to a fixed ambient temperature of 300 K) did not significantly change the results.

### 3.4 Solution Procedure

For each of the nine on-sun tests listed in Table 1, the FLUENT model was simulated until a converged solution was achieved for the continuity, velocity, energy, turbulence, and discrete-ordinates intensity residuals. The discrete-phase particle sources (momentum and heat sinks/sources generated by the particles and applied to the continuous phase equations) were updated every flow iteration, and one continuous phase iteration was applied per discrete-phase iteration. Ten flow iterations were run per radiation iteration. In some runs, the solar irradiation was omitted so that unheated particle velocities and concentrations could be compared to experimental measurements of the same quantities [10].

For the on-sun test comparisons, the particle and wall temperatures were used as metrics to calibrate the parameters that governed the shape (but not magnitude) of the solar irradiation entering through the solar patch. The irradiation beam width, beam direction, and diffuse fraction were varied until the comparisons between the predicted and measured particle and wall temperatures were qualitatively optimized. The following solar irradiation and discrete-ordinates radiation parameters yielded the best matches to the data:

- *Beam Width*:  $\theta$  (vertical) x  $\phi$  (horizontal) =  $30 \times 150$  degrees
- *Beam Direction*: (0, 0.5, -0.866) or 30 degrees from horizontal
- *Diffuse Fraction*: 0.15
- *Angular Discretization of Solid Angles*:  $\theta \times \phi$  divisions =  $7 \times 7$ ,  $\theta \times \phi$  pixels =  $3 \times 3$

The calibrated values for the simulated beam shape and direction were within the range of the actual beam shape entering the receiver as dictated by the number and location of heliostats used in each test. The angular discretization of the solid angles was refined sufficiently to yield smooth temperature and incident radiation distributions.

## 4. RESULTS AND DISCUSSION

Simulated results were compared to measured particle velocities, volume fractions, wall temperatures, and particle temperatures recorded during a series of unheated tests [10] and on-sun tests [11].

### 4.1 Particle Velocity and Concentration

Simulations of unheated particle velocity and concentration (volume of particles divided by total volume occupied by particles and air) were compared to measured

values from previous tests [10]. Figure 3 shows a plot of the simulated and measured particle velocities as a function of particle distance from the release point. Simulation results for two different mesh resolutions are shown, and both yield very similar results to the measured velocities (average relative error ~6%). The particle velocity increases rapidly after being released (reaching 4 m/s within 1 m of the release point), and continues to increase more slowly thereafter.

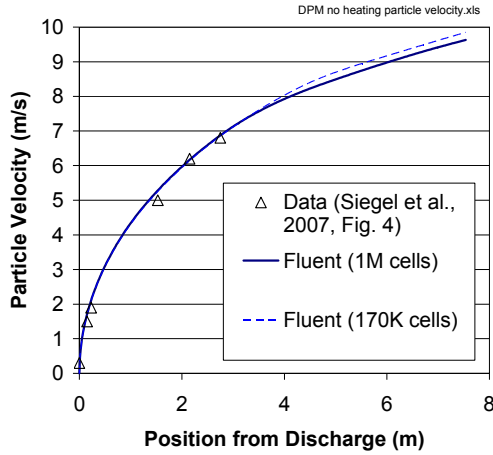


**Figure 3. Simulated vs. measured particle velocities for unheated test [10].**

Figure 4 shows a plot of the simulated and measured particle volume fraction at different locations beneath the release point [10]. As the particles fall downward, they disperse and decrease in concentration. The maximum volume fraction is less than 3% near the top, and decreases to less than 0.5% within 3 m from the release point. The average relative error between the simulated and measured particle volume fractions was ~8%.

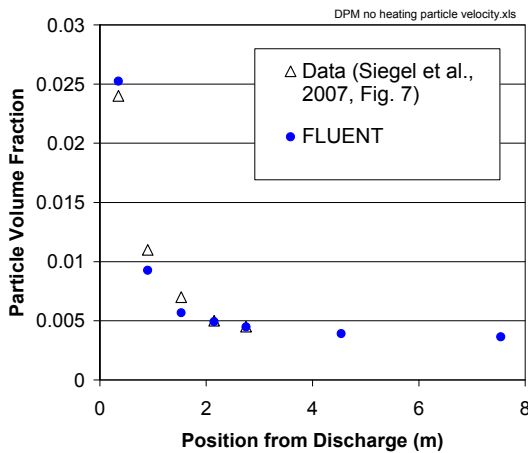


**Figure 4. Simulated vs. measured particle volume fraction for unheated test [10].**

## 4.2 On-Sun Test Comparisons

Figure 5 shows representative images from the simulations of the nine on-sun tests listed in Table 1. The left image shows the simulated incident radiation on the walls of the receiver. No “spillage” occurs on the front walls of the receiver because the source of the irradiation is the small patch in the center of the aperture. However, because the beam shape emanating from the patch was defined by vertical and horizontal angles of 30 and 150 degrees, respectively, with a diffuse fraction of 0.15, the solar flux is spread laterally and vertically on the walls. In addition, the direction of the beam is aligned 30 degrees above horizontal, so the beam enters the cavity in an upward direction. The simulated beam shape and direction is approximately the same as the actual concentrated flux entering the receiver based on the location of the heliostats used in the tests.

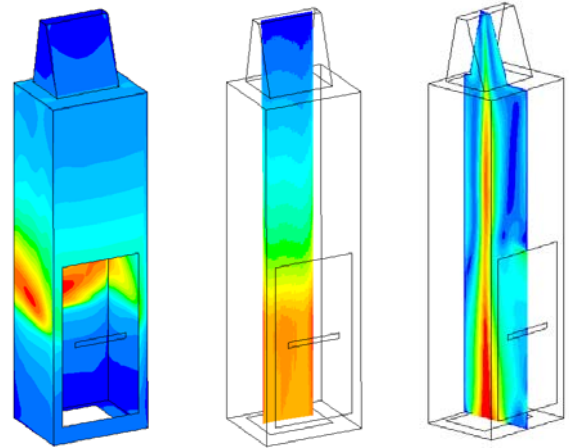


**Figure 5. Simulated wall incident radiation (left), particle tracks colored by temperature (middle), and gas flow colored by velocity (right).**

The middle image in Figure 5 shows simulated particle tracks (colored by temperature) of particle streams released along the discharge slot. As the particles pass near the aperture, they are irradiated by the concentrated solar flux and increase in temperature.

The right image in Figure 5 shows simulated contours of gas-phase velocity within the receiver. The falling particles entrain airflow downward (up to ~5 m/s). Air enters the receiver through the cavity and is pushed primarily downward with the particles, although some air entering the top of the aperture flows upward along the front wall before recirculating back down with the particle flow. Behind the particle curtain, hot air rises upward along the back wall and recirculates back down with the falling particles.

Figure 6 shows a plot of the simulated and measured vertical temperature distributions along the center of the back wall of the receiver for the test conducted on 2/22/08, which is representative of the wall temperature distribution for each test.

The wall temperature increases from the bottom of the receiver to a point approximately 2.3 m above the bottom. This is the point where the maximum solar flux was incident on the back wall. The location of the maximum temperature was used to calibrate the solar beam direction used in the simulations. Above this location, the temperature decreases with increasing height. Near the top of the cavity, the wall temperature begins to increase again slightly, probably due to lower convective heat transfer to the adjacent air flow, which has a lower buoyant upward velocity near the top of the receiver where the vertical wall meets the top wall.

The data in Figure 6 show that the measured wall temperatures were still increasing during the duration of the test. Nevertheless, the trend in the transient temperature distribution is similar to the simulated steady-state wall temperature distribution.

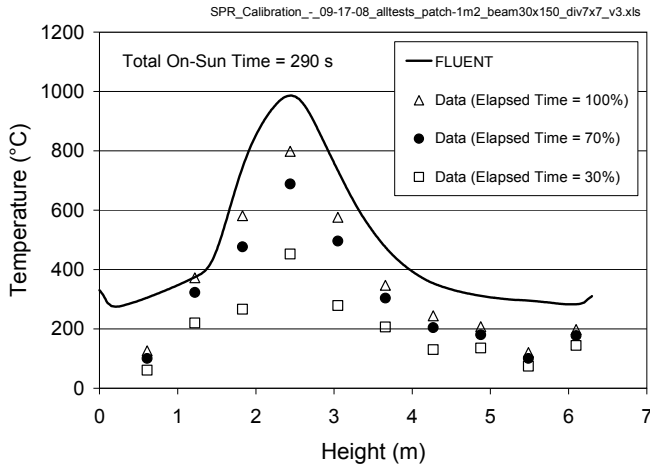


**Figure 6. Simulated and measured vertical temperature distributions along the center of the back wall of the receiver for the test conducted on 2/22/08 (5.32 kg/s-m, 2.56 MW).**

Figure 7 shows the simulated and measured increase in particle temperatures for all nine on-sun tests. The particle-temperature increase ranged from ~100 K – 250 K. As discussed in Siegel and Kolb [11], factors impacting the observed increase in particle temperatures included the input power and particle mass flow rate. Higher particle temperatures were observed during tests with higher input power and lower mass flow rates. It was postulated that at lower particle mass flow rates, less shading occurred with a lower concentration of particles, and the particles received more direct solar irradiation.

The measured increase in particle temperature is within the range of simulated values for eight out of the nine tests. The simulated particle-temperature increase follows the observed trends as a function of input power and particle mass flow rate. For a given mass flow rate, the simulated particle-temperature increase was positively correlated with simulated input power

(for example, compare the results for the two runs at 8.72 kg/s-m on 2/8/08). For a given input power, the simulated particle-temperature increase was negatively correlated with the particle mass flow rate (for example, compare the results of the runs at 2.56 MW on 2/18/08, 2/22/08, and 2/28/08).

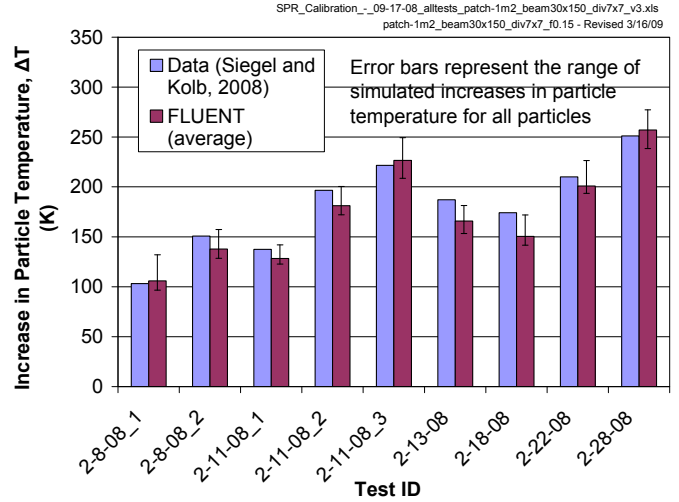


**Figure 7. Simulated vs. measured increase in particle temperatures for nine on-sun tests.**

Figure 8 shows the simulated and measured solid-particle-receiver efficiency for each test, where the efficiency is defined as follows:

$$\eta = \frac{Q_{particles}}{Q_{in}} = \frac{\sum_{i=1}^N \dot{m}_i c_p (T_{i,f} - T_{i,o})}{Q_{in}} \quad (1)$$

where  $\dot{m}_i$  is the mass flow rate of particle stream,  $i$ ,  $c_p$  is the particle specific heat (Table 3),  $T_{i,f}$  and  $T_{i,o}$  are the final and initial particle temperatures,  $Q_{particles}$  is the power absorbed by the particles, and  $Q_{in}$  is the total power entering the receiver (Table 1). The mass flow rate of each particle stream,  $i$ , is defined as the prescribed total mass flow rate (Table 1) divided by the number of particle streams tracked in the simulation (300).

Figure 9 and Figure 10 show the measured and simulated particle-temperature increase and receiver efficiencies as a function of input power (power into the aperture) for different particle mass flow rates. In general, the particle-temperature increase is greater with increasing input power, and the temperature increase is greater at lower flow rates. However, the receiver efficiency (Figure 10) is greatest at higher particle mass flow rates and higher input powers. As discussed in Siegel and Kolb [11], the efficiency improves with increasing particle mass flow rate at higher rates of input power (> 2.1 MW) due to the increased opacity of the particle curtain and its ability to intercept a greater fraction of the incident solar

energy. At lower flow rates, the opacity of the particle curtain is less and more solar flux is transmitted through the curtain to the back wall. Therefore, at higher input powers, the lower flow rates yield reduced efficiency. Interestingly, it appears that as the input power is reduced ( $< \sim 2$  MW), the efficiency of the high-flow-rate case (8.72 kg/s-m) begins to decrease below the efficiencies of the lower-flow-rate cases, possibly due to the increased particle shading and reduced particle-temperature increase. The interactions between these parameters and additional factors warrants a thorough parametric evaluation, which is currently underway.

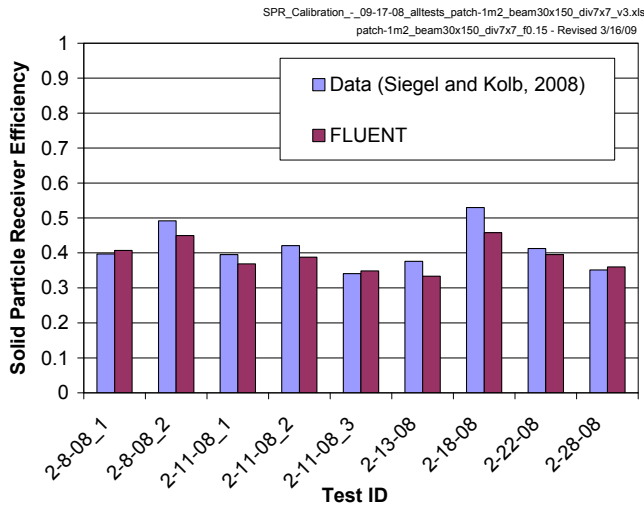


Figure 8. Simulated vs. measured solid-particle-receiver efficiency for nine on-sun tests.

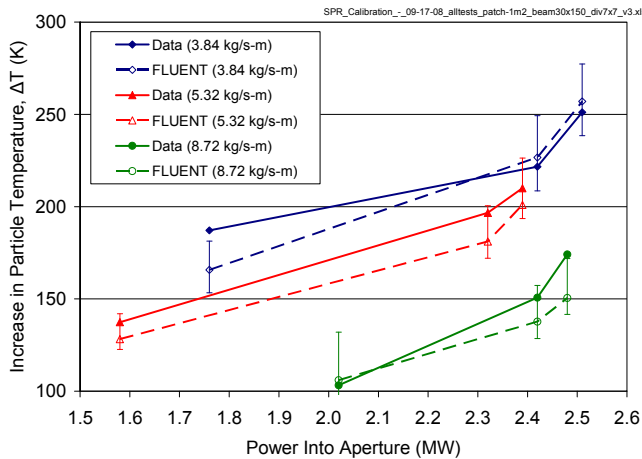


Figure 9. Simulated and measured increase in particle temperatures as a function of input power for different particle mass flow rates.

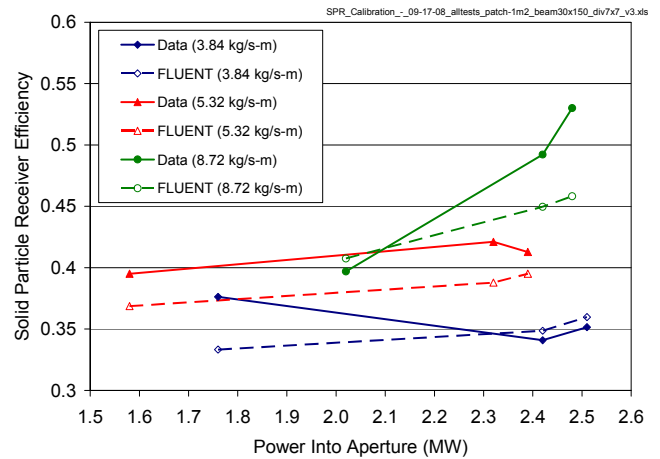


Figure 10. Simulated and measured receiver efficiencies as a function of input power for different particle mass flow rates.

## 5. CONCLUSIONS AND FUTURE WORK

A computational model of particle flow through a solid particle receiver has been developed. As the particles fall through the receiver cavity, they are irradiated by concentrated solar energy entering the receiver through an aperture. Solar irradiation, reradiation and emission from the cavity walls, convection, wall conduction, and two-phase particle/air flow are simulated in the model. Simulated results are compared to measured temperatures of the particles and walls during nine on-sun tests. Results are also compared to particle velocities and concentrations measured during unheated tests with good matches to the data. Results show that the model accurately predicts the salient distributions and trends in particle temperatures and efficiencies as a function of input power and particle mass flow rate. In general, the particle-temperature increase is greater with increasing input power, and the temperature increase is greater at lower flow rates. However, the receiver efficiency depends on both the particle mass flow rate and input power. At higher mass flow rates, the particle-curtain opacity is greater. This can intercept more solar flux at a higher input power, yielding higher efficiency, but it can also cause greater particle shading at a lower input power, which reduces the efficiency.

Additional parametric analyses using the calibrated model are being performed to improve the performance and efficiency of the solid particle receiver. Parameters such as particle-drop position, particle size, particle mass flow rate, and solar input power are being evaluated using the calibrated model developed in this paper. Interactions and confounding effects will also be investigated to determine an optimized design.

## ACKNOWLEDGMENTS

Sandia is a multiprogram laboratory operated by Sandia Corporation, a Lockheed Martin Company for the United States Department of Energy's National Nuclear Security Administration under contract DE-AC04-94AL85000. The United States Government retains and the publisher, by accepting the article for publication, acknowledges that the United States Government retains a non-exclusive, paid-up, irrevocable, world-wide license to publish or reproduce the published form of this manuscript, or allow others to do so, for United States Government purposes.

## REFERENCES

- [1] Kolb, G.J. and R.B. Diver, 2008, Screening Analysis of Solar Thermochemical Hydrogen Concepts, SAND2008-1900, Sandia National Laboratories, Albuquerque, NM ([http://infoserve.sandia.gov/sand\\_doc/2008/081900.pdf](http://infoserve.sandia.gov/sand_doc/2008/081900.pdf)).
- [2] Steinfeld, A., A. Imhof, and D. Mischler, 1992, Experimental Investigation of an Atmospheric-Open Cyclone Solar Reactor for Solid-Gas Thermochemical Reactions, *J. Solar Energy Engineering*, 114, 171-174.
- [3] Z'Graggen, A., P. Haueter, D. Trommer, M. Romero, J.C. de Jesus, and A. Steinfeld, 2006, Hydrogen production by steam-gasification of petroleum coke using concentrated solar power—II Reactor design, testing, and modelling, *International J. of Hydrogen Energy*, 31, 797-811.
- [4] Klein, H.H., J. Karni, R. Ben-Zvi, and R. Bertocchi, 2007, Heat transfer in a directly irradiated solar receiver/reactor for solid-gas reactions, *Solar Energy*, 81(10), 1227-1239.
- [5] Kolb, G.J., R.B. Diver, and N. Siegel, 2007, Central-Station Solar Hydrogen Power Plant, *J. Solar Energy Engr.*, 129, 179-183.
- [6] Hurby, J.M., B.R. Steele, and V.P. Burolla, 1984, Solid Particle Receiver Experiments: Radiant Heat Test, Sandia National Laboratories, SAND84-8251.
- [7] Evans, G.H., W.G. Houf, R. Greif, and C. Crowe, 1985, Numerical Modeling of a Solid Particle Solar Central Receiver, Sandia National Laboratories, SAND85-8249.
- [8] Falcone, P.K., J.E. Noring, and J.M. Hruby, 1985, Assessment of a Solid Particle Receiver for a High Temperature Solar Central Receiver System, Sandia National Laboratories, SAND85-8208.
- [9] Chen, H., Y. Chen, H.-T. Hsieh, and N. Siegel (2007). Computational Fluid Dynamics Modeling of Gas-Particle Flow within a Solid Particle Solar Receiver, *J. Solar Energy Engineering*, 129, 160-170.
- [10] Siegel, N., G. Kolb, K. Kim, V. Rangaswamy, and S. Moujaes, 2007, Solid Particle Receiver Flow Characterization Studies, ASME Energy Sustainability 2007, Long Beach, CA, June 20-27, 2007.
- [11] Siegel, N. and G. Kolb, 2008, Design and On-Sun Testing of a Solid Particle Receiver Prototype, ASME Energy Sustainability 2008, Jacksonville, FL, April 10-14, 2008.
- [12] Kistler, B.L., 1987, A User's Manual for DELSOL3: A Computer Code for Calculating the Optical Performance and Optimal System Design for Solar Thermal Central Receiver Plants, Sandia National Laboratories, Livermore, CA, [SAND86-8018 \(10 MB\)](#).
- [13] Touloukian, Y.S. and D.P. DeWitt, 1972, Thermal Radiative Properties Nonmetallic Solids, Thermophysical Properties of Matter Volume 8, Plenum Publishers, New York.
- [14] Incropera, F.P. and D.P. DeWitt, 1985, Introduction to Heat Transfer, John Wiley & Sons, New York, Table A.2.
- [15] Fluent Inc., 2006, Fluent 6.3 User's Guide, Fluent Inc., Lebanon, NH.
- [16] Shih, T.-H., W.W. Liou, A. Shabbir, Z. Yang, and J. Zhu., 1995, A New k- $\epsilon$  Eddy-Viscosity Model for High Reynolds Number Turbulent Flows - Model Development and Validation, *Computers Fluids*, 24(3):227-238.